

Power Generation from a Radiative Thermal Source Using a Large-Area Infrared Rectenna

Joshua Shank, Emil A. Kadlec, Robert L. Jarecki, Andrew Starbuck, Stephen Howell,
David W. Peters, and Paul S. Davids*

Sandia National Laboratories, Albuquerque, New Mexico 87185, USA

 (Received 20 December 2017; revised manuscript received 5 March 2018; published 25 May 2018)

Electrical power generation from a moderate-temperature thermal source by means of direct conversion of infrared radiation is important and highly desirable for energy harvesting from waste heat and micropower applications. Here, we demonstrate direct rectified power generation from an unbiased large-area nanoantenna-coupled tunnel diode rectifier called a rectenna. Using a vacuum radiometric measurement technique with irradiation from a temperature-stabilized thermal source, a generated power density of 8 nW/cm^2 is observed at a source temperature of $450 \text{ }^\circ\text{C}$ for the unbiased rectenna across an optimized load resistance. The optimized load resistance for the peak power generation for each temperature coincides with the tunnel diode resistance at zero bias and corresponds to the impedance matching condition for a rectifying antenna. Current-voltage measurements of a thermally illuminated large-area rectenna show current zero crossing shifts into the second quadrant indicating rectification. Photon-assisted tunneling in the unbiased rectenna is modeled as the mechanism for the large short-circuit photocurrents observed where the photon energy serves as an effective bias across the tunnel junction. The measured current and voltage across the load resistor as a function of the thermal source temperature represents direct current electrical power generation.

DOI: [10.1103/PhysRevApplied.9.054040](https://doi.org/10.1103/PhysRevApplied.9.054040)

I. INTRODUCTION

The conversion of electromagnetic radiation into electric current is the basis of electromagnetic detection [1,2], wireless power transfer [3–5], and solar-energy harvesting [1,6]. Photodetection and optical-to-electrical energy conversion typically rely on photon-induced conductive currents in semiconductor device structures. The thermal infrared region of the spectrum lies at a crossover point between optical photovoltaic conversion in photodiodes and direct power conversion through rectification in the radio-frequency region of the spectrum. Infrared square-law detectors and energy-conversion devices require small band-gap semiconductors matched to the infrared photon energy. At room temperature, these small band-gap semiconductors are in thermal equilibrium with a large number of thermally generated photons. Thermal source illumination from a higher-temperature source in the bandwidth of the detector must generate more photons than the equilibrium photon gas [7]. If photon flux from the thermal source does not outnumber these thermally generated photons in the device, then the signal is obscured by thermal noise and no useful work can be obtained from this device. This is a consequence of the second law of thermodynamics. For most infrared photodetection applications, these devices need to be cooled

to reduce the thermal background photons in order to produce a detected signal [2]. However, for this reason they are not good thermal-energy-harvesting devices for moderate-temperature sources.

Infrared direct detection based on rectification of the displacement current in a tunnel diode can reduce the need for device cooling but requires the ability to respond on the timescale of the oscillation of the infrared radiation. In the thermal infrared, this timescale corresponds to frequencies in the range of 20–50 THz, where carrier transport phenomena are typically too slow. Many research groups have examined ultrafast tunneling as a means of rectification and detection for optical frequencies [8–11]. Infrared rectennas have been extensively studied theoretically [12] and experimentally [13–15] using metal-insulator-metal tunnel diode rectifiers and antenna designs based on scaled versions of microwave antennas. However, these optical rectennas typically are operated under high-power laser illumination and applied dc bias and do not scale to a large area readily due to their fabrication using *e*-beam lithography. By utilizing complementary metal-oxide-silicon (CMOS) fabrication techniques, uniform high-yielding distributed tunnel diode rectenna can be fabricated over full wafers with diameters of 300 mm.

Tunneling diode rectifiers with high asymmetry are required to efficiently convert the small-signal infrared electric field amplitude in an unbiased diode into a

*pdavids@sandia.gov

photocurrent. Furthermore, the tunnel diode must be located near the concentrating infrared antenna to minimize Ohmic loss associated with metals in the infrared. This parasitic Ohmic absorption leads to an increase in the temperature of the device and reduces the conversion efficiency. In order to overcome these inefficiencies, nano-antenna and metasurface design concepts are developed to create distributed tunnel diode rectifiers to resonantly concentrate the infrared electric field in the tunnel barrier for enhanced tunneling.

Previously, we demonstrated room-temperature photo-response of large-area 1D and 2D nanoantenna-coupled tunnel diodes under coherent infrared illumination in biased and unbiased operation [16,17]. The infrared photo-response was attributed to the large field enhancement in the spectral region near the epsilon-near-zero (ENZ) material resonance of the oxide tunnel barrier leading to enhanced tunneling rectification. In this paper, we examine a 1D rectenna under thermal source illumination in a vacuum radiometry experimental setup. We demonstrate power generation across a load resistance and discuss photon-assisted tunneling in the unbiased device and optimization for thermal power supplies.

II. EXPERIMENT

Vacuum radiometry is a technique used to measure photothermal response of thermophotovoltaics and infrared rectennas under thermal illumination. The experimental setup is shown schematically in Fig. 1(a), where a ceramic heater with an integrated temperature controller acts as a thermal source of radiation. The heater is shrouded by a water-cooled coil, and the emissivity of the heater is approximately 90% across the thermal infrared band. The purpose of the water-cooled shroud is to shield the surroundings from the heater and to avoid creating secondary thermal sources with large thermal time constants. The packaged rectenna sample shown in Fig. 1(b) is mounted to a large water-cooled copper block that acts as a thermal ground and electrically connected to a ribbon cable for electrical characterization. The cooled rectenna assembly is mounted to a linear stage which controls the distance between the thermal source and device under test. The stages are not precise enough for repeatable power versus distance measurements and, therefore, they are held fixed at 2–3 mm spacing for all temperature measurements. Thermocouples are attached to the sample to monitor the temperature.

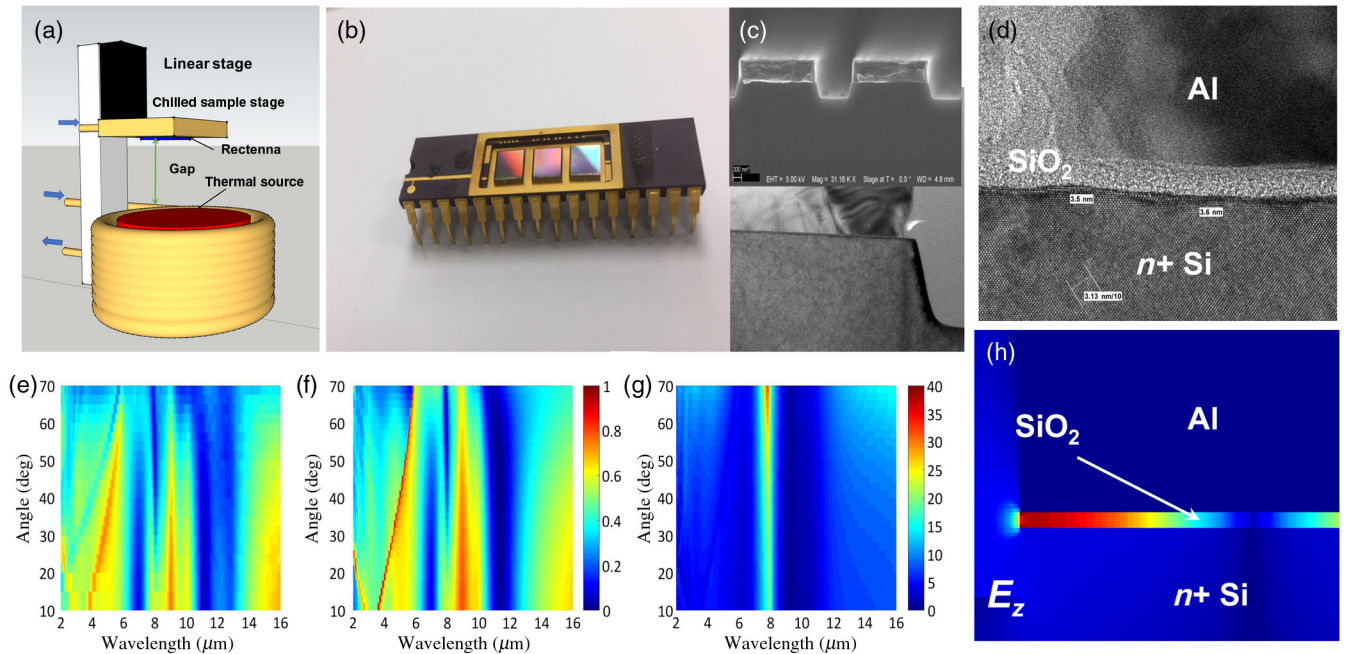


FIG. 1. Schematic of vacuum radiometric measurement for thermal source irradiation of a large-area infrared rectenna. (a) The schematic shows a water-cooled shroud around a temperature-controlled ceramic thermal heater that acts as a thermal source. A packaged rectenna with active area $3 \times 3 \text{ mm}^2$ shown in (b) is attached to a chilled large Cu block that is on a linear stage that controls the source-rectenna distance. The temperature of the rectenna and the Cu block are monitored with attached thermocouples. (c) The large-area rectenna is an integrated nanoantenna-coupled metal-oxide-semiconductor tunnel diode that has been described previously [16,17]. (d) High-resolution TEM shows the tunnel diode cross section highlighting the oxide thickness ($\approx 3\text{--}4 \text{ nm}$). The entire large-area nanoantenna-coupled tunnel diode is encapsulated in thick oxide. (e) Simulated (f) measured TM reflectance spectra from the rectenna. Units: 0 (no reflectance), 1 (complete reflectance). (g) Simulated peak field concentration factor $\gamma = E_z^{\text{gap}}/E_0$ in the rectenna. (h) The z -directed transverse field concentration in tunnel oxide at resonance. The z axis is perpendicular to the tunnel barrier.

The large-area rectenna structure has been previously described [16] and consists of an integrated, large-area metal-grating antenna structure with a metal-oxide-semiconductor tunnel diode shown in Figs. 1(c) and 1(d). The grating is designed to effectively confine and enhance thermal infrared radiation into a (3–4)-nm tunnel barrier. Figure 1(e) shows the simulated and measured [Fig. 3(f)] transverse-magnetic reflectance for the rectenna. A large absorption resonance is seen in the region near the oxide longitudinal optical phonon resonance at $8.1 \mu\text{m}$. The transverse field enhancement is shown in Fig. 1(g) as a function of the wavelength and incident angle, and the field enhancement profile near resonance at $7.3 \mu\text{m}$ [Fig. 1(h)] is shown from simulation. At normal incidence, the field enhancement factor is approximately $10 - 15\times$ the incident field amplitude. The transverse field enhancement in the tunneling barrier is seen to increase for oblique incidence.

The electrical characterization of the rectenna is shown schematically in Fig. 2(a) and illustrates the device under blackbody illumination in vacuum. The blackbody spectral

exitance incident on the rectenna is shown in Fig. 2(b) for the source-temperature range considered. The spectral exitance is the illuminated power per unit area per unit bandwidth and can be compared to the Poynting vector flux irradiating the rectenna where the gray band indicates the absorption resonance on the rectenna. Explicitly, the spectral exitance M_ν^0 is given by

$$M_\nu^0(T) = \frac{2\pi h\nu^3}{c^2} \frac{1}{\exp(\beta h\nu) - 1}, \quad (1)$$

where $\beta = 1/k_B T$, h is Planck's constant, c is the speed of light, and ν is the photon frequency. From the spectral exitance, the incident photon field amplitude E_0 is derived from its relationship with the Poynting vector flux incident onto the device. As we see, the transverse electric field amplitude in the barrier is enhanced relative to the incident field $E_z^{\text{gap}} = \gamma E_0$ in the spectral region near the ENZ resonance and is given by $E_z^{\text{gap}} = \gamma[2Z_0 M_\nu^0(T) d\nu]^{1/2}$, where Z_0 is the impedance of free space, $d\nu$ is the

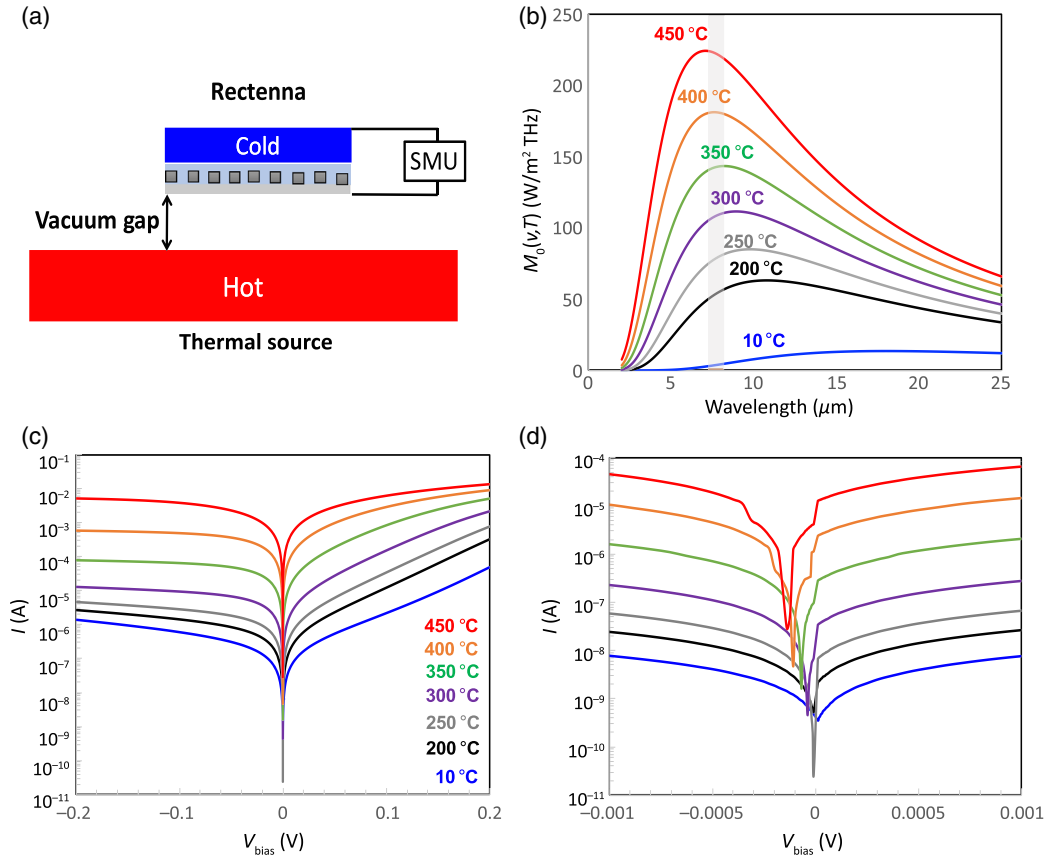


FIG. 2. *Rectenna I-V characteristics under thermal source irradiation.* (a) The schematic of vacuum radiometric measurement of the *I-V* characteristics of the rectenna under thermal source illumination. (b) Spectral blackbody exitance for the blackbody source in the temperature range considered for the experiment. (c) *I-V* sweeps of the rectenna at varying thermal source temperatures. (d) High-resolution *I-V* characteristics around zero bias showing the current minimum shifting into the second quadrant as the thermal source temperature increases. Note: Thermocoupled measurement of the rectenna does not show any significant heating of the device or the Cu thermal sink. In all plots, the source-temperature color map: 200 °C (black), 250 °C (gray), 300 °C (purple), 350 °C (green), 400 °C (gold), and 450 °C (red) lines.

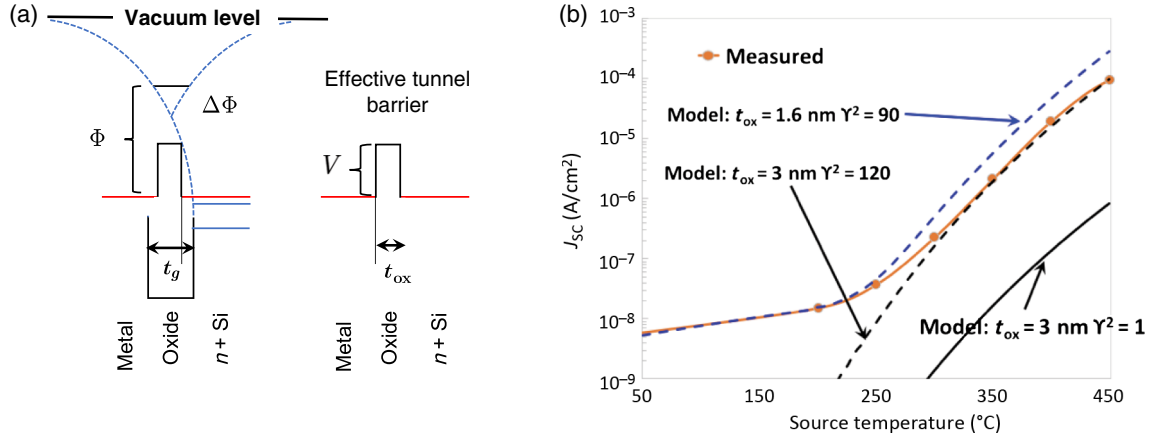


FIG. 3. *Short-circuit rectenna current density as a function of the source temperature.* (a) Schematic band diagram of an n -type MOS tunnel diode with Schottky image potential lowering of the tunnel barrier shown in blue dashed lines. The resulting effective barrier height is given by $\Phi - \Delta\Phi$ and the width is shown. Here, t_g is the physical device thickness and t_{ox} is the effective device thickness. (b) Measured and modeled short-circuit current density for various effective barrier conditions. $\Phi = 3.0$ eV and $t_g = 4.0$ nm for the Al/SiO₂/ n^+ Si MOS device. In all modeling, $V = 1.65$ eV, and the effective oxide thickness $t_{ox} = 3$ nm. The longitudinal effective masses are $m_l = m_e$, $m_r = 0.19m_e$, and $m_{ox} = 0.5m_e$ where m_e is the bare electron mass.

bandwidth, and γ represents the transverse field enhancement factor in the tunnel barrier. Figures 2(c) and 2(d) show the current-voltage characteristics for the thermally illuminated rectenna for source temperatures in the range of room temperature to 450 °C. The I - V data indicate large changes in the rectenna conductance as the source temperature is increased. Furthermore, the I - V near-zero bias shows that the open-circuit voltage change shifts from zero to negative voltage indicating rectification occurring in the second quadrant. The large increase in tunneling conductance accompanies the change in diode asymmetry as the temperature increases, and we observe large short-circuit currents at zero bias.

Photon-assisted tunneling is a well-established process in superconducting tunnel junctions [18–21] and has been observed in semiconductor superlattices [22]. The short-circuit tunneling current can be modeled by considering photon-assisted tunneling within the transfer Hamiltonian model for a uniform barrier tunneling under zero bias. The nanoantenna n -type MOS tunnel diode band diagram can be modeled as a uniform barrier that is reduced by Schottky image potential lowering yielding an effective barrier height and tunneling thickness. Reductions in effective barrier height and thicknesses for MOS tunnel diodes on degenerately doped Si substrates have been extensively examined [23] and image potential lowering calculations can affect the computed tunnel currents [24]. Figure 3(a) shows the band diagram for the n -type MOS tunnel diode illustrating the impact of image force lowering of the barrier on both sides of the device. The bulk barrier height $\Phi = 3.0$ eV is lowered by 1.35 eV, and the effective tunneling distance at the Fermi level is reduced from the metallurgical thickness of approximately 4.0 nm to an effective tunnel thickness of 3.0 nm. Photon-assisted tunneling is a

dynamical tunneling effect, where the image charges are induced on the metal and semiconductor surfaces and dynamically screened at terahertz rates. Therefore, the image potential calculation uses the dynamic frequency-dependent permittivity in the resonance band of nanoantenna for the computation for the effective barrier parameters. In Appendix A, the analytic image potential calculation is derived. Figure 5 shows schematically the iterative image potential calculation which is used as a zero parameter fit to compute the short-circuit current. The other parameters in the computation are the spectral absorption and the field concentration in the tunnel barrier which are determined from electromagnetic simulations. Figure 3(b) shows the measured short-circuit current as a function of the source temperature. An observable increase in the short-circuit current occurs near a source temperature of $T \simeq 250$ °C, where the peak of the blackbody spectral exitance shown in Fig. 2(b) crosses the rectenna spectral resonance.

The expression for the single-photon contribution to the short-circuit current density is [25]

$$J^{(1)} = AT^2 \left(\frac{m_r m_l}{m_{ox}^2} \right) 2Z_0 \int_{\nu_{min}}^{\nu_{max}} d\nu (1 - R^2) \times \gamma^2 \left(\frac{e t_{ox}}{h\nu} \right)^2 M_\nu^0(T) \mathcal{T}(\nu), \quad (2)$$

where $A = 120$ A/cm²K² is Richardson's constant, $1 - R^2$ is the frequency-dependent nanoantenna absorption,

$$\mathcal{T}(\nu) = \beta \int dE_l t(E_l, E_l + h\nu) \ln \left[\frac{1 + e^{-\beta E_l}}{1 + e^{-\beta(E_l + h\nu)}} \right] \quad (3)$$

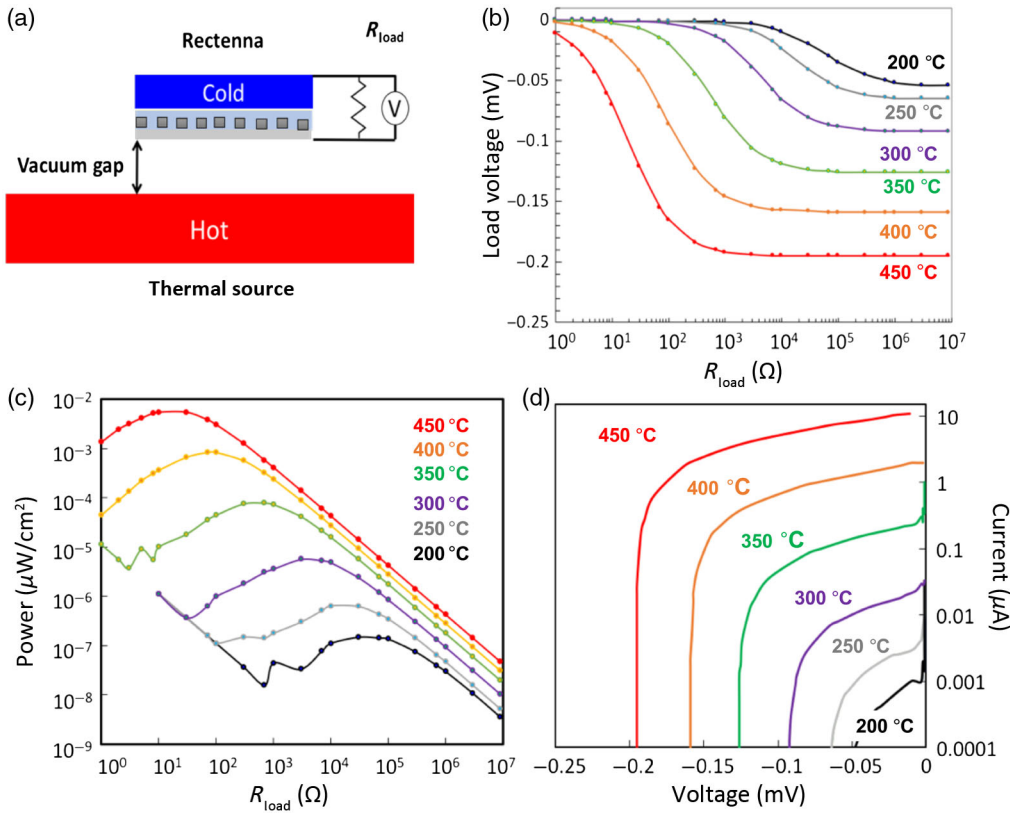


FIG. 4. Power generation from a thermal source in an external load resistor. (a) Schematic of the vacuum radiometry experiment for power generation. The gap is held fixed at ≈ 2 mm for all measurements. (b) Measured load voltage as a function of the load resistance for the source temperature ranging from 200 to 450 °C. (c) Power generation as a function of the load resistance for various source temperatures. (d) Load diagram in the second quadrant illustrating the current and voltage in the load resistor as a function of the source temperature. In all plots, the source temperature color map: 200 °C (black), 250 °C (gray), 300 °C (purple), 350 °C (green), 400 °C (gold), and 450 °C (red) lines.

is the integrated barrier transmission, and $h\nu$ is the photon energy that acts as an effective bias in the supply function. The transfer Hamiltonian barrier transmittance is

$$t(E_l, E_r) = e^{-(k+q)t_{ox}} \sinh^2 \left(\frac{(k-q)t_{ox}}{2} \right), \quad (4)$$

where the first term has the form of the standard tunneling exponential, and the second term is the square hyperbolic sinc function. The evanescent wave vectors in the barrier region are $k = [2m_l(V - E_l)/\hbar^2]^{1/2}$ and $q = [2m_r(V - E_r)/\hbar^2]^{1/2}$ as defined in the caption. The modeled zero-bias current density is shown in Fig. 3(b) with various field concentration factors and effective oxide thicknesses. The modeled results accurately predict the temperature transition and the short-circuit current density above the transition temperature for realistic effective barrier height, thicknesses, and computed field enhancement factors for normal incidence.

Finally, we come to the ultimate goal of electrical power generation from radiated heat from a thermal source. Figure 4(a) shows the configuration for the power generation measurement. An external variable resistive load is placed across the thermally illuminated large rectenna and a voltage is recorded. In the experiment, the thermal source-rectenna vacuum gap of ≈ 2 –3 mm is fixed for all measurements, and the external resistor board is outside

the vacuum at room temperature. Thus, the measurement is in the far field of the thermal source, and due to the large size difference between the heater and the rectenna, the view factor is approximately unity out to large angles of incidence. The measured voltage and current are recorded, and the electrical power delivered to the load resistor is computed. Figure 4(b) shows the measured load voltage across the load resistor as the source temperature is varied. The measured voltage is seen to saturate at the open-circuit voltage as the resistance is increased. At the highest source temperature of 450 °C, the measured voltage is 0.2 mV for resistances above 2 k Ω . Figure 4(c) shows the electrical power generated as the load resistance is varied for a set of thermal source operating conditions. The electrical power generation increases to a maximum at a select load resistance for each source temperature. The peak power is seen to shift to lower resistance values as the source temperature is increased. The peak load resistance matches and tracks the tunnel diode resistance at zero bias indicative of direct rectification impedance matching requirements. Electrical rectification from an ac signal requires that the diode impedance match the load impedance for maximum power transmission to the load. The current-voltage load diagram is shown in Fig. 4(d). The power generation is clearly in the second quadrant, and photogenerated currents of 10 μA and voltages of tenths of a millivolt are obtained at the higher source temperatures.

III. CONCLUSIONS

In summary, we unambiguously generate electrical power from a radiative thermal source at moderate temperatures. The measured currents and voltages across a load impedance are indicative of direct rectification of infrared radiation in our unbiased large-area nanoantenna-coupled tunnel diode. The peak power load resistance is seen to precisely match the tunnel diode resistance at zero volts, consistent with antenna rectifier impedance matching conditions.

A model of broadband photon-assisted tunneling through an effective tunnel barrier is proposed and quantitatively matches the short-circuit current over three decades [25]. The model includes realistic field concentration in the tunnel barrier as observed under finite-element modeling of the electromagnetic response of the device. This high field in the tunnel barrier gives rise to the large short-circuit currents and can be tuned through the design of the metasurface resonance [26–28] and the material optical phonon modes [29].

In this paper, we report electrical power generation from an incoherent broadband thermal source. Previously, we estimated the power conversion efficiency of our rectenna at $\approx 0.01\%$ under direct quantum-cascade laser illumination [16]. The power conversion efficiency estimation under incoherent thermal illumination is inaccurate since it requires measurement of the source and rectenna emissivity, source and rectenna surface temperature, radiometric view factor, and separation. Here, the absolute power per unit area generation under no external bias across a load resistance is the preferred figure of merit. While the power generation seems modest, the large-area fill factor can compensate for low efficiency conversion and improvements in the device design, and improvements in the device performance can be readily implemented within a standard CMOSi process. The result will be a micropower supply that can convert radiated waste heat into useable electric power for wide-ranging applications.

ACKNOWLEDGMENTS

Funding for this work is provided by Sandia’s Laboratory Directed Research and Development Program. Sandia National Laboratories is a multimission laboratory managed and operated by National Technology and Engineering Solutions of Sandia, a wholly owned subsidiary of Honeywell International Inc., for the United States Department of Energy’s National Nuclear Security Administration under Contract No. DE-NA0003525.

APPENDIX A: IMAGE POTENTIAL BARRIER LOWERING

The tunneling barrier shape, height V , and width t_{gap} are modified by the metal image potential in the metal-insulator degenerately doped Si tunnel diode [24]. To solve for the electric potential of an electron in the tunnel barrier, we use the method of images to compute the potential ϕ and the electric energy $W = q\phi/2$ at the position of a test charge in the dielectric region of a *MIM* diode. Figure 5(a) shows the configuration for a charge $-q$ at position x . The image charges are placed to make the two surfaces equipotential surfaces, and this process can be iterated. The resulting image potential energy is

$$W = -\frac{q^2}{8\pi\epsilon_0\epsilon} \left\{ \sum_{n=1}^{\infty} \left(\frac{nt}{(nt)^2 - x^2} - \frac{1}{nt} \right) + \frac{1}{2x} \right\}, \quad (\text{A1})$$

and the effective barrier $\Phi_e(x) = \Phi + W(x)$. The oxide barrier height is set at the bulk barrier for Al on SiO₂, $\Phi = 3.0$ eV. The image potential lowered barrier $\Phi_e(x)$ is shown in Fig. 5(b) and can be converted into an effective rectangular barrier by integration. We obtain

$$Vt_{\text{ox}} = \int_{x_0}^{x_1} dx \Phi_e(x), \quad (\text{A2})$$

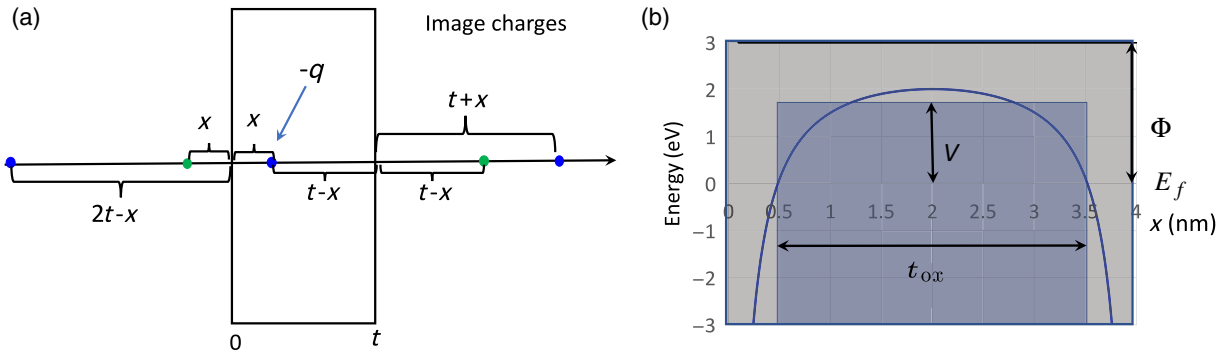


FIG. 5. *Image potential calculation and effective barrier height and width.* (a) Method of image solution for a charge located at position x from the left metal contact after the second stage for the metal-vacuum-metal structure. (b) Image potential lowered barrier and effective rectangular barrier are shown. The bulk Al/SiO₂ barrier height is 3.0 eV, and the gap thickness is 4 nm. The effective uniform barrier height is 1.65 eV and the thickness is 3 nm.

where $\Phi_e(x_0) = 0$ and $\Phi_e(x_1) = 0$ are the intersections of the barrier at $E_f = 0$. Typically, the relative permeability for the oxide is used in the calculation, but in the rectenna device the tunneling is dynamic. The enhanced electric field in the barrier is inducing image charges at 30 THz, and it, therefore, makes sense to use the dispersive infrared permittivity in the calculation. In the infrared resonance band, ϵ varies from $1 \rightarrow 0$, so for the calculation of the effective uniform barrier, we use $\epsilon = 1/2$. From the above discussion, the effective uniform barrier height $V = 1.65$ eV and the effective oxide thickness $t_{\text{ox}} = 3$ nm as described in the main text.

APPENDIX B: IMPEDANCE MATCH

The conditions of impedance matching are well developed in rectified detection and power sources. Antenna-matching networks are used to reduce reflection from the antenna to maximize power to the rectifying diode, and a second matched network is used to maximize power to the load impedance. In the rectenna, the diode rectifier is distributed and integrated into the antenna surface. The rectenna is optimized to have low reflectance in the region where we have high field enhancement in the tunnel barrier. The condition for maximal power generation occurs when the load resistance matches the tunnel diode resistance at zero bias. Figure 6 shows that the rectenna satisfies the impedance matching condition. Typically, one achieves peak power delivered to the load when the diode impedance matches the load impedance. The peak power load resistance matches the tunnel diode resistance at $V = 0$ as a function of the source temperature over many decades of resistance. This clearly indicates that the power generation arises from rectification and not from bolometric or internal thermoelectric effects.

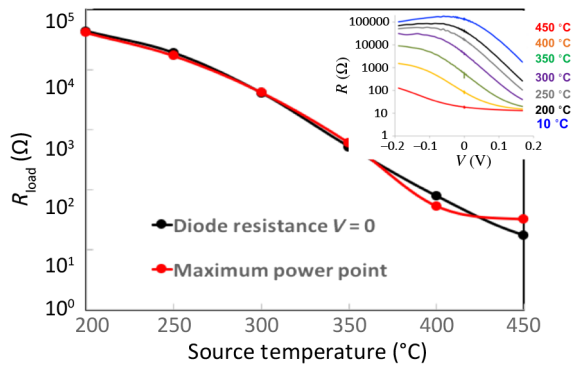


FIG. 6. Impedance matching and diode resistance versus source temperature. Load resistance (left) at peak power generation as a function of the source temperature. The diode resistance (inset) as a function of applied voltage under illumination from a thermal source. The diode resistance at zero bias for each source temperature is also plotted in the left panel.

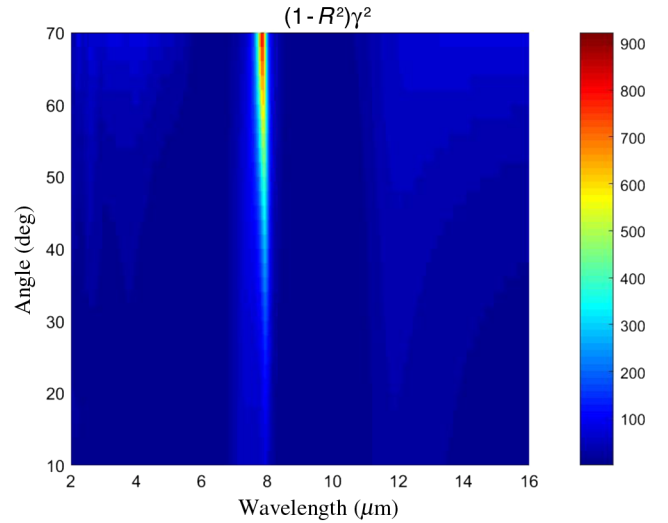


FIG. 7. Figure of merit for resonant field enhancement. The computed figure of merit as a function of the incident angle and wavelength for the grating nanoantenna structure outlined in the paper.

APPENDIX C: FIGURE OF MERIT

The figure of merit $F(\theta, \lambda) = (1 - R^2)\gamma^2$ represents the field enhancement in the tunnel gap weighted by the absorption of the nanoantenna and is in the integrand for the photon-assisted tunnel current expression Eq. (2). In the computed short-circuit current model, we use fixed normal incidence values for the figure of merit. Ideally, we want high absorption in the nanoantenna structure and high field concentration in the tunnel gap. These are competing requirements since the field concentration in the tunnel gap occurs very close to the ENZ longitudinal optical phonon mode of the oxide. It is difficult to obtain zero reflection from the oxide overcoated structure near the ENZ point. Figure 7 shows the computed figure of merit for the nanoantenna structure of the paper as a function of the angle and wavelength. It is instructive to note that at large angles we get the largest figure of merit near the ENZ resonance of $8.1 \mu\text{m}$ for the oxide. This field enhancement is sizeable for oblique incidence near the well-known Berreman-guided-mode resonance [30]. This implies that power generation at oblique incidence will be significant, and we can optimize the view factor to improve the conversion efficiency.

- [1] Simon M. Sze and Kwok K. Ng, *Physics of Semiconductor Devices* (John Wiley & Sons, New York, 2006).
- [2] E. L. Dereniak and Glenn D. Boreman, *Infrared Detectors and Systems*, Wiley Series in Pure and Applied Optics (John Wiley & Sons, New York, 1996).
- [3] J. A. Hagerty, F. B. Helmbrecht, W. H. McCalpin, R. Zane, and Z. B. Popovic, Recycling ambient microwave energy

- with broad-band rectenna arrays, *IEEE Trans. Microwave Theory Tech.* **52**, 1014 (2004).
- [4] Young-Ho Suh and Kai Chang, A high-efficiency dual-frequency rectenna for 2.45- and 5.8-GHz wireless power transmission, *IEEE Trans. Microwave Theory Tech.* **50**, 1784 (2002).
- [5] James O. McSpadden, Lu Fan, and Kai Chang, Design and experiments of a high-conversion-efficiency 5.8-GHz rectenna, *IEEE Trans. Microwave Theory Tech.* **46**, 2053 (1998).
- [6] Kunta Yoshikawa, Hayato Kawasaki, Wataru Yoshida, Toru Irie, Katsunori Konishi, Kunihiro Nakano, Toshihiko Uto, Daisuke Adachi, Masanori Kanematsu, Hisashi Uzu, and Kenji Yamamoto, Silicon heterojunction solar cell with interdigitated back contacts for a photoconversion efficiency over 26%, *Nat. Energy* **2**, 17032 (2017).
- [7] P. T. Landsberg and G. Tonge, Thermodynamic energy conversion efficiencies, *J. Appl. Phys.* **51**, R1 (1980).
- [8] Daniel R. Ward, Falco Hüser, Fabian Pauly, Juan Carlos Cuevas, and Douglas Natelson, Optical rectification and field enhancement in a plasmonic nanogap, *Nat. Nanotechnol.* **5**, 732 (2010).
- [9] Sachit Grover, Olga Dmitriyeva, Michael J. Estes, and Garret Moddel, Traveling-wave metal/insulator/metal diodes for improved infrared bandwidth and efficiency of antenna-coupled rectifiers, *IEEE Trans. Nanotechnol.* **9**, 716 (2010).
- [10] Asha Sharma, Virendra Singh, Thomas L. Bougher, and Baratunde A. Cola, A carbon nanotube optical rectenna, *Nat. Nanotechnol.* **10**, 1027 (2015).
- [11] S. Piltan and D. Sievenpiper, Optical rectification using geometrical field enhancement in gold nano-arrays, *J. Appl. Phys.* **122**, 183101 (2017).
- [12] A. Sanchez, C. F. Davis, K. C. Liu, and A. Javan, The MOM tunneling diode: Theoretical estimate of its performance at microwave and infrared frequencies, *J. Appl. Phys.* **49**, 5270 (1978).
- [13] M. Bareiß, P. M. Krenz, G. P. Szakmany, B. N. Tiwari, D. Kälblein, A. O. Orlov, G. H. Bernstein, G. Scarpa, B. Fabel, U. Zschieschang, H. Klauk, W. Prod, and P. Lugli, Rectennas revisited, *IEEE Trans. Nanotechnol.* **12**, 1144 (2013).
- [14] Edgar Briones, Javier Alda, and Francisco Javier González, Conversion efficiency of broad-band rectennas for solar energy harvesting applications, *Opt. Express* **21**, A412 (2013).
- [15] M. N. Gadalla, M. Abdel-Rahman, and Atif Shamim, Design, optimization and fabrication of a 28.3 THz nano-rectenna for infrared detection and rectification, *Sci. Rep.* **4**, 4270 (2014).
- [16] Paul S. Davids, Robert L. Jarecki, Andrew Starbuck, D. Bruce Burckel, Emil A. Kadlec, Troy Ribaud, Eric A. Shaner, and David W. Peters, Infrared rectification in a nanoantenna-coupled metal-oxide-semiconductor tunnel diode, *Nat. Nanotechnol.* **10**, 1033 (2015).
- [17] Emil A. Kadlec, Robert L. Jarecki, Andrew Starbuck, David W. Peters, and Paul S. Davids, Photon-Phonon-Enhanced Infrared Rectification in a Two-Dimensional Nanoantenna-Coupled Tunnel Diode, *Phys. Rev. Applied* **6**, 064019 (2016).
- [18] P. K. Tien and J. P. Gordon, Multiphoton process observed in the interaction of microwave fields with the tunneling between superconductor films, *Phys. Rev.* **129**, 647 (1963).
- [19] John Bardeen, Tunneling into Superconductors, *Phys. Rev. Lett.* **9**, 147 (1962).
- [20] M. H. Cohen, L. M. Falicov, and J. C. Phillips, Superconductive Tunneling, *Phys. Rev. Lett.* **8**, 316 (1962).
- [21] A. H. Dayem and R. J. Martin, Quantum Interaction of Microwave Radiation with Tunneling between Superconductors, *Phys. Rev. Lett.* **8**, 246 (1962).
- [22] B. J. Keay, S. J. Allen, J. Galán, J. P. Kaminski, K. L. Campman, A. C. Gossard, U. Bhattacharya, and M. J. W. Rodwell, Photon-Assisted Electric Field Domains and Multiphoton-Assisted Tunneling in Semiconductor Superlattices, *Phys. Rev. Lett.* **75**, 4098 (1995).
- [23] L. A. Kasprzak, R. B. Laibowitz, and M. Ohring, Dependence of the Si-SiO₂ barrier height on SiO₂ thickness in MOS tunnel structures, *J. Appl. Phys.* **48**, 4281 (1977).
- [24] N. M. Miskovsky, P. H. Cutler, T. E. Feuchtwang, and A. A. Lucas, The multiple-image interactions and the mean-barrier approximation in MOM and MVM tunneling junctions, *Appl. Phys. A* **27**, 139 (1982).
- [25] Paul S. Davids and Joshua Shank, Density matrix approach to photon-assisted tunneling in the transfer Hamiltonian formalism, *Phys. Rev. B* **97**, 075411 (2018).
- [26] Xianliang Liu, Tatiana Starr, Anthony F. Starr, and Willie J. Padilla, Infrared Spatial and Frequency Selective Metamaterial with Near-Unity Absorbance, *Phys. Rev. Lett.* **104**, 207403 (2010).
- [27] Andrea Alù, Mário G. Silveirinha, Alessandro Salandrino, and Nader Engheta, Epsilon-near-zero metamaterials and electromagnetic sources: Tailoring the radiation phase pattern, *Phys. Rev. B* **75**, 155410 (2007).
- [28] J. B. Pendry, L. Martín-Moreno, and F. J. Garcia-Vidal, Mimicking surface plasmons with structured surfaces, *Science* **305**, 847 (2004).
- [29] Salvatore Campione, Sheng Liu, Alexander Benz, John F. Klem, Michael B. Sinclair, and Igal Brener, Epsilon-Near-Zero Modes for Tailored Light-Matter Interaction, *Phys. Rev. Applied* **4**, 044011 (2015).
- [30] D. W. Berreman, Infrared absorption at longitudinal optic frequency in cubic crystal films, *Phys. Rev.* **130**, 2193 (1963).